JOURNAL OF AIRCRAFT
Vol. 45, No. 2, March–April 2008

Flight Dynamics of Highly Flexible Aircraft

Chong-Seok Chang* and Dewey H. Hodges†
Georgia Institute of Technology, Atlanta, Georgia 30332-1510
and
Mayuresh J. Patil‡
Virginia Polytechnic Institute and State University, Blacksburg, Virginia 24061-0203

DOI: 10.2514/1.30890

An analysis and parametric study of the flight dynamics of highly flexible aircraft are presented. The analysis extends previous work of the authors, used to predict the atypical flight dynamic characteristics of highly flexible flying wings, to conventional configurations with one or more fuselages, wings, and/or tails. The aircraft structure is represented as a collection of geometrically exact, intrinsic beam elements, with continuity conditions enforced where beams intersect. The structural model is coupled with an aerodynamic model consisting of two-dimensional, large-angle-of-attack, unsteady theory for the lifting surfaces, and a fuselage model based on application of slender-body theory to a cylindrical beam. Influences of various design parameters such as wing flexibility, horizontal/vertical tail aerodynamics, and offset are investigated for aeroelasticity and flight dynamics of highly flexible aircraft. Results for prototype configurations illustrate the relationships between its design parameters and flight dynamic behavior.

Nomenclature

B	=	deformed-beam reference B frame
C^{iB}	=	rotation matrix from B frame to i
F	=	internal force measures in the B frame
g	=	gravity vector measures in the B frame
H	=	angular momentum measures
i	=	inertial frame
M	=	internal moment measures in the B frame
P	=	linear momentum measures
V	=	velocity measures in the B frame
$\hat{x}$	=	nodal variables
$\bar{x}$	=	element variables
γ	=	internal force strain measures
$\overline{\delta u}$	=	virtual displacement
$\overline{\delta \psi}$	=	virtual rotation
κ	=	internal moment strain measures
Ω	=	angular velocity measures in the B frame

I. Introduction

HIGH-ALTITUDE, long-endurance (HALE) aircraft are being developed for various missions, including environmental science research, telecommunication relay service, and military reconnaissance missions. Among such aircraft, the solar-powered Helios (manufactured by Aerovironment, Inc.) flew at an altitude of 96,863 ft. Such aircraft are envisioned to become atmospheric satellites, with missions spanning several months or even years.

One significant difference between such aircraft and conventional aircraft is that they operate with large wing deflections, because they typically have highly flexible wings with a high aspect ratio. Zerweckh et al. [1] first indicated the unusual flight dynamic behavior of a human-powered aircraft having a high-aspect-ratio wing ($AR \approx 40$). They developed a fully flexible aeroelastic model [2] to analyze its aeroelastic behavior and to compare the test data with the pretest analysis. The phugoid mode was mildly unstable. They recommended that structural flexibility and unsteady aerodynamics be included in any future preliminary design analysis.

Before this work, Waszak and Schmidt [3] investigated the effects of structural flexibility on the modal characteristics of flexible airplane. They compared the frequency responses of residualized models of different orders (eliminating higher-order aeroelastic effects). It showed that the frequency separation between rigid-body modes and elastic modes becomes less obvious as flexibility increases. This work was extended to high-fidelity simulation of flexible aircraft using a modal-based model [4].

Various numerical simulations were developed to investigate the aeroelastic behavior of flexible aircraft. Patil et al. [5] investigated the nonlinear aeroelasticity and flight dynamics, taking into account the structural geometric nonlinearity and unsteady flow. Their results indicated that the elastic modes with low frequencies affected the phugoid mode as well as the short-period mode. They extended the work to nonlinear aeroelastic stability analysis [6] and the design of an output feedback controller to suppress flutter and alleviate gust loads [7]. Recently, Patil and Hodges [8] developed the computer code called nonlinear aeroelastic trim and stability of HALE aircraft (NATASHA), based on previous theoretical work in which governing equations are the geometrically exact equations of motion [9] written in their intrinsic form, augmented with intrinsic kinematical equations [10]. NATASHA correctly predicts the unusual flight dynamic behavior of certain HALE configurations [8].

Drela [11] also presented an integrated simulation model called ASWING for flexible aircraft. ASWING aims to conduct rapid modeling and flight simulation of such aircraft by investigating nonlinear static and dynamic response with gust fields and by stability analysis. Meirovitch and Tuzcu [12] developed a unified theory of maneuvering flexible aircraft and applied it to time-history simulation [13], focusing on dynamic characteristics and designing a linear feedback controller. Their formulation was extended from a previous development of hybrid equations of motion [14], which combines rigid-body and flexible subsystems for modeling a satellite with elastic appendages.

Garcia [15] coupled an Euler/Navier–Stokes computational fluid dynamic analysis to a beam finite element model and investigated the nonlinear aeroelastic behavior of high-aspect-ratio wings. Numerical results for both unswept and swept wing cases, with linear and nonlinear structural representation, are compared and discussed for the tip stall characteristics. Reference [16] studied the HALE

Received 8 March 2007; revision received 5 July 2007; accepted for publication 2 September 2007.

*Postdoctoral Fellow, School of Aerospace Engineering. Member AIAA.
†Professor, School of Aerospace Engineering. Fellow AIAA.
‡Assistant Professor, Department of Aerospace and Ocean Engineering. Senior Member AIAA.

joined-wing aircraft as a NASTRAN finite element model coupled with an Euler/Navier–Stokes CFD solver.

II. Structural Model

The fundamental structural modeling approach uses the intrinsic beam formulation, which elegantly accounts for all geometrical nonlinearity. The governing equations are the geometrically exact equations of motion [9] written in their intrinsic form. However, instead of being augmented by the kinematical relations therein, which relate generalized strain and velocity measures to temporal and spatial partial derivatives of displacement and rotation variables, they are augmented by the intrinsic kinematical equations derived in [10]. The latter development has advantages: It does not require a modal-based linear model (often used in other works [3,13]), the level of complexity is reduced because displacement and rotational variables are not involved in the governing equations, and the highest degree of nonlinearity is only two.

A. Intrinsic Beam Formulation

The geometrically exact, intrinsic governing equations [9] for the dynamics of a general, nonuniform, twisted, curved, and anisotropic beam are

$$\begin{aligned} F_B' + \widetilde{K_B} F_B + f_B &= \dot{P}_B + \widetilde{\Omega_B} P_B \\ M_B' + \widetilde{K_B} M_B + (\widetilde{e_1} + \tilde{\gamma}) F_B + m_B &= \dot{H}_B + \widetilde{\Omega_B} H_B + \widetilde{V_B} P_B \\ V_B' + \widetilde{K_B} V_B + (\widetilde{e_1} + \tilde{\gamma}) \Omega_B &= \dot{\gamma} \\ \Omega_B' + \widetilde{K_B} \Omega_B &= \dot{\kappa} \end{aligned} \tag{1}$$

where column matrices F_B and M_B contain the internal force and moment measures; P_B and H_B are the sectional linear and angular momenta; V_B and Ω_B are the velocity and angular velocity measures; γ and κ are the beam force and moment strain measures; $K_B = k_b + \kappa$ are the deformed-beam twist and curvature measures; k_b are the undeformed-beam initial twist and curvature measures; f_B and m_B are the external distributed forces and moments from gravity, aerodynamics, and controls; and $e_1^T = \lfloor 1 \quad 0 \quad 0 \rfloor$. The quantities with $\widetilde{\ }$ accents are 3×3 antisymmetric matrices associated with the 3×1 column matrices such that $\tilde{\bullet}_{32} = -\tilde{\bullet}_{23} = \bullet_1$, $\tilde{\bullet}_{13} = -\tilde{\bullet}_{31} = \bullet_2$, and $\tilde{\bullet}_{21} = -\tilde{\bullet}_{12} = \bullet_3$.

A central-difference discretization scheme is applied to the intrinsic governing equations in space to obtain a numerical solution. The scheme satisfies both of the space–time conservation laws derived in [10]. The finite difference scheme can be viewed as equivalent to a particular finite element discretization, and the intrinsic governing equations are expressed as element and nodal equations. The nth element equations, which are a discretized form of Eq. (1), are

$$\begin{aligned} &\frac{\hat{F}_l^{n+1} - \hat{F}_r^n}{\mathrm{d}l} + (\widetilde{\bar{\kappa}^n} + \widetilde{\bar{k}^n})\bar{F}^n + \bar{f}^n - \dot{\bar{P}}^n - \widetilde{\bar{\Omega}^n}\bar{P}^n = 0 \\ &\frac{\hat{M}_l^{n+1} - \hat{M}_r^n}{\mathrm{d}l} + (\widetilde{\bar{\kappa}^n} + \widetilde{\bar{k}^n})\bar{M}^n + (\widetilde{\bar{e}_1} + \widetilde{\bar{\gamma}^n})\bar{F}^n + \bar{m}^n - \dot{\bar{H}}^n \\ &\quad - \widetilde{\bar{\Omega}^n}\bar{H}^n - \widetilde{\bar{V}^n}\bar{P}^n = 0 \\ &\frac{\hat{V}_l^{n+1} - \hat{V}_r^n}{\mathrm{d}l} + (\widetilde{\bar{\kappa}^n} + \widetilde{\bar{k}^n})\bar{V}^n + (\widetilde{\bar{e}_1} + \widetilde{\bar{\gamma}^n})\bar{\Omega}^n - \dot{\bar{\gamma}}^n = 0 \\ &\frac{\hat{\Omega}_l^{n+1} - \hat{\Omega}_r^n}{\mathrm{d}l} + (\widetilde{\bar{\kappa}^n} + \widetilde{\bar{k}^n})\bar{\Omega}^n - \dot{\bar{\kappa}}^n = 0 \end{aligned} \tag{2}$$

where $\bar{f}^n$ and $\bar{m}^n$ include any external forces and moments applied to the nth element.

The equations for node n need to include possible discontinuities due to a nodal mass, a nodal force, and slope discontinuity, so that

$$\begin{aligned} \hat{F}_r^n - \hat{C}_{lr}^{n^T}\hat{F}_l^n + \hat{f}^n - \dot{\hat{P}}_r^n - \widetilde{\hat{\Omega}_r^n}\hat{P}_r^n = 0 \\ \hat{M}_r^n - \hat{C}_{lr}^{n^T}\hat{M}_l^n + \hat{m}^n - \dot{\hat{H}}_r^n - \widetilde{\hat{\Omega}_r^n}\hat{H}_r^n - \widetilde{\hat{V}_r^n}\hat{P}_r^n = 0 \end{aligned} \tag{3}$$

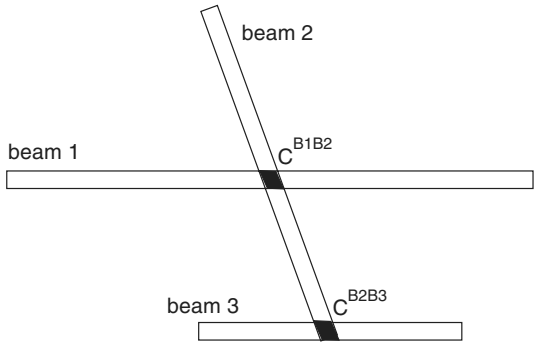

Fig. 1 Representation of conventional aircraft into a multiple-beam structure.

where $\hat{C}_{lr}^n$ reflects the slope discontinuity, $\hat{f}^n$ and $\hat{m}^n$ are external forces and moments applied at the nth node, and

$$\hat{V}_l^n = \hat{C}_{lr}^n \hat{V}_r^n \qquad \hat{\Omega}_l^n = \hat{C}_{lr}^n \hat{\Omega}_r^n \tag{4}$$

B. Multiple-Beam Formulation

A conventional aircraft frequently can be represented as a multiple-beam structure. For modeling a conventional aircraft as a multiple-beam structure, the intrinsic beam formulation needs to be extended to model fuselages, horizontal and vertical tails, and other structures as additional beam elements.

What follows is a brief description of how the intrinsic beam formulation can be extended to treat a multiple-beam configuration. As an example, conventional aircraft longitudinal dynamics can be regarded as consisting of three beams: namely, a flexible wing, a flexible fuselage, and a flexible horizontal tail, as shown in Fig. 1. These beams will share a node from which the flexible wing and horizontal tail are connected to the fuselage. This yields the following relations for virtual displacement and rotational variables defined at the common node of beams 1 and 2:

$$\overline{\delta u}_{\text{beam1}} = C^{B_1B_2}\overline{\delta u}_{\text{beam2}} \qquad \overline{\delta \psi}_{\text{beam1}} = C^{B_1B_2}\overline{\delta \psi}_{\text{beam2}} \tag{5}$$

where $C^{B_1B_2}$ is the rotation matrix from B_2 (reference frame of beam 2 at the common node) to B_1 (reference frame of beam 1 at the common node).

The nodal equations associated with the virtual displacements $\overline{\delta u}_{\text{beam1,2}}$ and rotations $\overline{\delta \psi}_{\text{beam1,2}}$ at the common node will be summed up as one set of nodal equations using Eqs. (5). As separate beams, the nodal equations for beam 1 are

$$\begin{aligned} \hat{F}_r^n - \hat{C}_{lr}^{n^T}\hat{F}_l^n + \hat{\mu}^n \hat{g}_r^n + \hat{f}^n - \dot{\hat{P}}_r^n - \widetilde{\hat{\Omega}_r^n}\hat{P}_r^n = 0 \\ \hat{M}_r^n - \hat{C}_{lr}^{n^T}\hat{M}_l^n + \hat{\mu}^n \widetilde{\hat{\xi}^n}\hat{g}_r^n + \hat{m}^n - \dot{\hat{H}}_r^n - \widetilde{\hat{\Omega}_r^n}\hat{H}_r^n - \widetilde{\hat{V}_r^n}\hat{P}_r^n = 0 \end{aligned} \tag{6}$$

For beam 2, they are

$$\begin{aligned} \hat{F}_b^m - \hat{C}_{fb}^{m^T}\hat{F}_f^m + \hat{\mu}^m \hat{g}_b^m + \hat{f}^m - \dot{\hat{P}}_b^m - \widetilde{\hat{\Omega}_b^m}\hat{P}_b^m = 0 \\ \hat{M}_b^m - \hat{C}_{fb}^{m^T}\hat{M}_f^m + \hat{\mu}^m \widetilde{\hat{\xi}^m}\hat{g}_b^m + \hat{m}^m - \dot{\hat{H}}_b^m - \widetilde{\hat{\Omega}_b^m}\hat{H}_b^m - \widetilde{\hat{V}_b^m}\hat{P}_b^m = 0 \end{aligned} \tag{7}$$

If two beams are connected to each other, this will reduce the separate nodal equations as follows:

$$\begin{aligned} &\hat{F}_r^n - \hat{C}_{lr}^{n^T}\hat{F}_l^n + \hat{\mu}^n \hat{g}_r + \hat{f}^n - \dot{\hat{P}}_r^n - \widetilde{\hat{\Omega}_r^n}\hat{P}_r^n + C^{B_1B_2}(\hat{F}_b^m - \hat{C}_{fb}^{m^T}\hat{F}_f^m) = 0 \\ &\hat{M}_r^n - \hat{C}_{lr}^{n^T}\hat{M}_l^n + \hat{\mu}^n \widetilde{\hat{\xi}^n}\hat{g}_r + \hat{m}^n - \dot{\hat{H}}_r^n - \widetilde{\hat{\Omega}_r^n}\hat{H}_r^n - \widetilde{\hat{V}_r^n}\hat{P}_r^n \\ &\quad + C^{B_1B_2}(\hat{M}_b^m - \hat{C}_{fb}^{m^T}\hat{M}_f^m) = 0 \end{aligned} \tag{8}$$

Several terms such as $\hat{\mu}^m \hat{g}_b^m$, $\hat{f}^m$, $\hat{P}_b^m$, $\hat{m}_T^m$, $\hat{\mu}^m \widetilde{\hat{\xi}^m} \hat{g}_b^m$, $\hat{m}^m$, and $\hat{H}_b^m$ in beam 2 are dropped from the separate nodal equation because they become redundant if beams 1 and 2 are taken as main and subordinate beams, respectively. So the nodal equation counts as only one set of governing equations (losing six nodal equations). But the lost six equations are compensated by the continuity conditions at the common node:

$$\hat{V}^{\,n}_{\text{beam1}} = C^{B_1 B_2} \hat{V}^m_{\text{beam2}} \qquad \hat{\Omega}^n_{\text{beam1}} = C^{B_1 B_2} \hat{\Omega}^m_{\text{beam2}} \tag{9}$$

C. Gravity Equation

The external force and moments in Eq. (1) include any external loads applied to the beam, such that

$$\begin{aligned} f_B &= f_{\text{aero}} + f_{\text{control}} + f_g + f_T \\ m_B &= m_{\text{aero}} + m_{\text{control}} + m_g + m_T \end{aligned} \tag{10}$$

where f_{aero} and m_{aero} are aerodynamic loads, f_{control} and m_{control} are the force and moment generated by control surfaces, f_g and m_g are force and moment by gravity expressed as $f_g = \mu g$ and $m_g = \mu \tilde{\xi} g$, and f_T and m_T are force and moment generated by thrust.

If the gravitational force is included into the analysis, the formulation needs additional equations. A unit gravity vector g is known in the inertial frame and has column matrix $\lfloor 0 \;\; 0 \;\; -1 \rfloor^T$ when expressed in inertial basis. However, the governing equations are described in the deformed-beam cross-sectional reference frame. The gravity vector measures have to satisfy the following differential equations in space and time:

$$g' + (\tilde{\kappa} + \tilde{k}) g = 0 \qquad \dot{g} + \tilde{\Omega} g = 0 \tag{11}$$

The corresponding discretized forms are

$$\frac{\hat{g}_l^{n+1} - \hat{g}_r^n}{\mathrm{d}l} + (\widetilde{\bar{\kappa}^n} + \widetilde{k^n}) \bar{g}_r^n = 0 \qquad \dot{\hat{g}}_r^n + \widetilde{\hat{\Omega}_r^n} \hat{g}_r^n = 0 \tag{12}$$

If the column matrix of gravity vector measures in the deformed-beam cross-sectional reference frame is known at one node, then the column matrices at other nodes and in time can be obtained from Eq. (12). In addition, the gravity vector measures also should satisfy the unit-vector measure condition

$$|\hat{g}_r^n| = 1 \tag{13}$$

which replaces one of the dynamic equations of Eq. (12) at the reference node, providing a boundary condition to determine a trim condition [see Eq. (15)].

Additionally, for multiple-beam configuration, the boundary condition for the gravity vector at the reference node for beam 2 is replaced by the continuity condition at the common node. This is calculated by

$$\hat{g}^{\,n}_{\text{beam1}} = C^{B_1 B_2} \hat{g}^m_{\text{beam2}} \tag{14}$$

D. Boundary Conditions

The following boundary conditions complete the structural formulation for the flight dynamics of a highly flexible aircraft. For beam 1, the boundary conditions are

$$\begin{gathered} \hat{F}_l^1 = 0 \qquad \hat{M}_l^1 = 0 \qquad \hat{F}_r^{N+1} = 0 \qquad \hat{M}_r^{N+1} = 0 \\ (e_1 e_1^T + e_2 e_2^T) \dot{\hat{g}}_r^n + (e_1 e_1^T + e_2 e_2^T) \widetilde{\hat{\Omega}_r^n} \hat{g}_r^n + (e_3 e_3^T) |\hat{g}_r^n| = e_3 \end{gathered} \tag{15}$$

where $|\hat{g}_r^n| = \sqrt{(g_1^n)^2 + (g_2^n)^2 + (g_3^n)^2}$, and g_i^n is the ith component in the nth set of gravity vector measures.) For beam 2 in a multiple-beam configuration, the boundary conditions are

$$\begin{gathered} \hat{F}_f^1 = 0 \qquad \hat{M}_f^1 = 0 \qquad \hat{F}_b^{M+1} = 0 \qquad \hat{M}_b^{M+1} = 0 \\ \hat{g}_{\text{beam1}} = C^{B_1 B_2} \hat{g}_{\text{beam2}} \end{gathered} \tag{16}$$

where M is the total number of elements for beam 2.

III. Aerodynamic Model

In this section, the separate types of aerodynamic models for wings/tails versus fuselages are described.

A. Wing and Tail Aerodynamic Model

A 2-D aerodynamic model is used to evaluate the aerodynamic forces and moments generated by lifting or control surfaces such as wings, flaps, and elevators. The unsteady effect is included in the analysis by using the inflow theory of Peters et al. [17]

The lift and drag forces at the quarter-chord and pitching moment about the quarter-chord are given from [8]

$$\begin{aligned} L^n_{\text{aero}} &= \rho b_n (V_T^n)^2 (C^n_{l_0} + C^n_{l_\alpha} \sin\alpha^n + C^n_{l_\beta} \beta^n) \\ &\quad + \rho b_n V_T^n V^n_{a_2} C^n_{l_\alpha} \alpha^n_{\text{rot}} \cos\alpha^n \\ D^n_{\text{aero}} &= \rho b_n (V_T^n)^2 C^n_{d_0} + \rho b_n V_T^n V^n_{a_2} C^n_{l_\alpha} \alpha^n_{\text{rot}} \sin\alpha^n \\ M^n_{\text{aero}} &= 2\rho b_n^2 (V_T^n)^2 (C^n_{m_0} + C^n_{m_\alpha} \sin\alpha^n + C^n_{m_\beta} \beta^n) - \rho b_n^2 V_T^n V^n_{a_2} C^n_{l_\alpha} \frac{\alpha^n_{\text{rot}}}{2} \end{aligned} \tag{17}$$

where

$$V_T^n = \sqrt{(V^n_{a_2})^2 + (V^n_{a_3})^2} \tag{18}$$

$$\sin\alpha^n = \frac{-V^n_{a_3}}{V_T^n} \tag{19}$$

$$\alpha^n_{\text{rot}} = \frac{\Omega^n_{a_1} (b_n/2)}{V_T^n} \tag{20}$$

where $V^n_{a_2}$ and $V^n_{a_3}$ are the corresponding column matrix components of $\bar{V}^n_a$ in the aerodynamic frame, β^n is the flap deflection of the nth element of the wing, and for a horizontal tail, the terms associated with β^n should be replaced by γ^n (that is, the elevator deflection of the nth element of horizontal tail).

The lift, drag, and pitching moments of Eq. (17) are now expressed in the aerodynamic frame basis, yielding

$$\begin{aligned} f^n_a &= \begin{Bmatrix} 0 \\ -L^n_{\text{aero}} \frac{V^n_{a_3}}{V_T^n} - D^n_{\text{aero}} \frac{V^n_{a_2}}{V_T^n} \\ L^n_{\text{aero}} \frac{V^n_{a_2}}{V_T^n} - D^n_{\text{aero}} \frac{V^n_{a_3}}{V_T^n} \end{Bmatrix} \\ &= \rho b_n \begin{Bmatrix} 0 \\ -(C^n_{l_0} + C^n_{l_\beta} \beta^n) V_T^n V^n_{a_3} + C^n_{l_\alpha} (V^n_{a_3})^2 - C^n_{d_0} V_T^n V^n_{a_2} \\ (C^n_{l_0} + C^n_{l_\beta} \beta^n) V_T^n V^n_{a_2} - C^n_{l_\alpha} V^n_{a_2} \left(V^n_{a_3} - \Omega^n_{a1} \frac{b_n}{2} \right) - C^n_{d_0} V_T^n V^n_{a_3} \end{Bmatrix} \\ m^n_a &= \begin{Bmatrix} M^n_{\text{aero}} \\ 0 \\ 0 \end{Bmatrix} \\ &= 2\rho b_n^2 \begin{Bmatrix} (C^n_{m_0} + C^n_{m_\beta} \beta^n)(V_T^n)^2 - C^n_{m_\alpha} V_T^n V^n_{a_3} - b_n \frac{C^n_{l_\alpha}}{8} V^n_{a_2} \Omega^n_{a_1} \\ 0 \\ 0 \end{Bmatrix} \end{aligned} \tag{21}$$

The column matrices of force and moment measures in the aerodynamic frame are transformed into the beam reference frame to be added as aerodynamic loads in the element equation (2). Thus,

$$\bar{f}^{\,n}_{\text{aero}} = C^n_a f^n_a \tag{22}$$

$$\bar{m}^{\,n}_{\text{aero}} = C^n_a m^n_a + C^n_a \tilde{y}^n_{ac} f^n_a \tag{23}$$

For unsteady effects, the inflow and acceleration terms are also included in the previous quasi-steady 2-D aerodynamics. The aerodynamic force and moment can be written as

$$f^n_a = \rho b_n \begin{Bmatrix} 0 \\ -(C^n_{l_0} + C^n_{l_\beta}\beta^n)V^n_T V^n_{a_3} + C^n_{l_\alpha}(V^n_{a_3} + \lambda^n_0)^2 - C^n_{d_0} V^n_T V^n_{a_2} \\ (C^n_{l_0} + C^n_{l_\beta}\beta^n)V^n_T V^n_{a_2} - C^n_{l_\alpha}\dot{V}_{a_3}\frac{b}{2} - C^n_{l_\alpha} V^n_{a_2}\left(V^n_{a_3} + \lambda^n_0 - \Omega^n_{a1}\frac{b_n}{2}\right) - C^n_{d_0} V^n_T V^n_{a_3} \end{Bmatrix} \tag{24}$$

$$m^n_a = 2\rho b^2_n \begin{Bmatrix} (C^n_{m_0} + C^n_{m_\beta}\beta^n)(V^n_T)^2 - C^n_{m_\alpha} V^n_T V^n_{a_3} - b_n \frac{C^n_{l_\alpha}}{8} V^n_{a_2}\Omega^n_{a_1} - C^n_{l_\alpha}\left(\frac{b^2_n}{32}\dot{\Omega}^n_{a_1} - \frac{b_n}{8}\dot{V}^n_{a_3}\right) \\ 0 \\ 0 \end{Bmatrix} \tag{25}$$

The inflow λ_0 is evaluated using the model of Peters et al. [17], such that

$$\begin{gathered} [A_{\text{inflow}}]\{\dot{\lambda}^n\} + \left(\frac{V^n_T}{b_n}\right)\{\lambda^n\} = \left(-\dot{V}^n_{a_3} + \frac{b_n}{2}\dot{\Omega}^n_{a1}\right)\{c_{\text{inflow}}\} \\ \lambda^n_0 = \frac{1}{2}\{b_{\text{inflow}}\}^T\{\lambda^n\} \end{gathered} \tag{26}$$

where λ^n is a column matrix of inflow states for the nth element and $[A_{\text{inflow}}]$, $\{b_{\text{inflow}}\}$, and $\{c_{\text{inflow}}\}$ are constant matrices given as

$$\begin{gathered} [A_{\text{inflow}}] = [D_{\text{inflow}} + d_{\text{inflow}} b^T_{\text{inflow}} + c_{\text{inflow}} d^T_{\text{inflow}} + \tfrac{1}{2} c_{\text{inflow}} b^T_{\text{inflow}}] \\ \{b_{\text{inflow}}\}_i = (-1)^{n-1}\frac{(N_i + i)!}{(N_i - i)!}\frac{1}{(i!)^2} \\ \{c_{\text{inflow}}\}_i = \frac{2}{i} \\ \{d_{\text{inflow}}\}_i = \frac{1}{2} \qquad (i \neq 1) \\ \{d_{\text{inflow}}\}_i = 0 \qquad (i = 1) \\ [D_{\text{inflow}}]_{ij} = \frac{i}{2} \qquad (i = j + 1) \\ [D_{\text{inflow}}]_{ij} = -\frac{i}{2} \qquad (i = j - 1) \\ [D_{\text{inflow}}]_{ij} = 0 \qquad (i \neq j \pm 1) \end{gathered} \tag{27}$$

where $\{X\}_i$ is the ith component of column matrix X, $[X]_{ij}$ is the ith row and jth column of matrix X, and N_i is the number of inflow states in the nth element ($i, j = 1, \ldots, N_i$).

B. Fuselage Aerodynamic Model

When the formulation is extended to incorporate the fuselage of a conventional aircraft configuration, an additional aerodynamic model is needed. The aerodynamic model follows the formulation of [11], so that

$$\begin{aligned} f^n_{\text{lift}} &= \rho \bar{V}^n_\perp \bar{V}^n_1 2\pi R(s)\frac{\mathrm{d}R(s)}{\mathrm{d}s} \\ f^n_{\text{drag}} &= -\tfrac{1}{2}\rho|\bar{V}^n|\bar{V}^n 2R(s)c_{\,\mathrm{d}f} - \tfrac{1}{2}\rho|\bar{V}^n_\perp|\bar{V}^n_\perp 2R(s)c_{\,\mathrm{d}p} \end{aligned} \tag{28}$$

where $R(s)$ is the fuselage radius that is a function of s, s is a scalar that indicates the distance along the fuselage reference line from the fuselage nose to the point at which the element fuselage aerodynamic forces are evaluated, $\bar{V}^n_1 = \bar{V}^{nT} e_1$ is the first component of the column matrix of the velocity measures, $\bar{V}^n_\perp = \bar{V}^n - \bar{V}^n_1 e_1$ is the column matrix of velocity measures perpendicular to the fuselage reference line, $c_{\mathrm{d}p}$ is the drag coefficient of a circular cylinder, and $c_{\mathrm{d}f}$ is comparable with the skin friction coefficient c_f. Note that $\bar{f}^n$ and $\bar{m}^n$ in Eq. (2) will include these aerodynamic loads in place of the loads formulated in the last subsection for wing aerodynamic loads if the element is a fuselage.

IV. Numerical Results

The following numerical results show how the developed structural and aerodynamic models can be applied to the analysis of highly flexible aircraft in both a flying-wing configuration and a conventional aircraft configuration.

A. Payload Distribution and Deformed Wing Shape

A primary characteristic of highly flexible aircraft, especially for those with a flying-wing configuration, is that they require a bit of wing dihedral for lateral stability because they do not have a vertical tail and built-in sweep angle. Moreover, due to the high wing flexibility, the deformed wing shape, payload distribution, and location of the center of gravity are coupled to each other.

In the first numerical study, the relation between the payload distribution and the deformed wing shape is investigated. If the total

Table 1 Base-configuration parameters

Parameters	Values	Units
Magnitude of aircraft forward velocity	20	m/s
Flight path angle	0	rad
Payload	17.75	kg

Table 2 Base-configuration properties

Properties		Wing	Units
m	Mass per unit length	0.75	kg/m
ℓ	Total length	66	m
$d\ell$	Element length	3	m
r/c	Radius/chord length	1	m
GJ	Torsional stiffness	1.0×10^4	Nm^2
EI_2	Vertical bending stiffness	3.0×10^5	Nm^2
EI_3	Chordwise bending stiffness	4.0×10^6	Nm^2

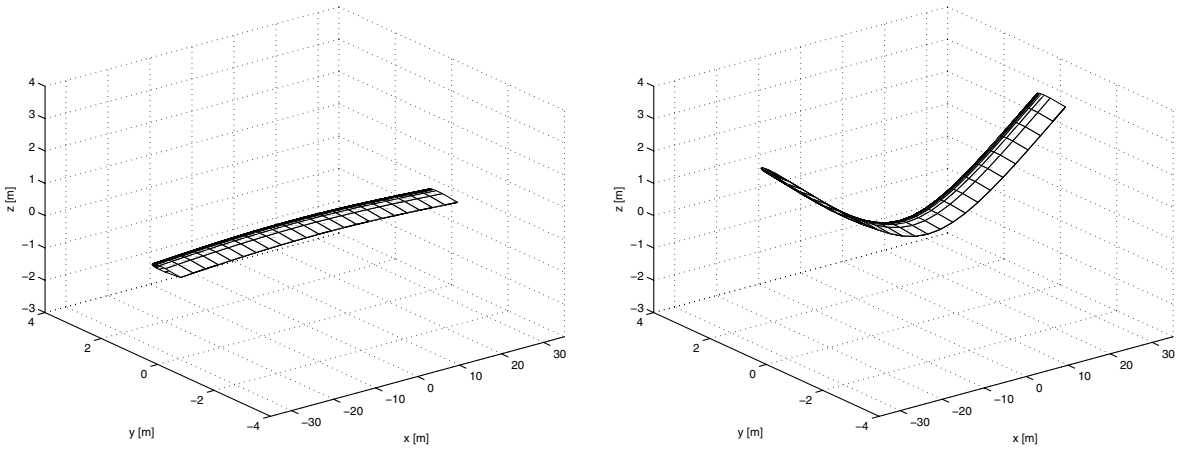

Fig. 2 Trim configuration of cases 1 (left) and 2 (right).

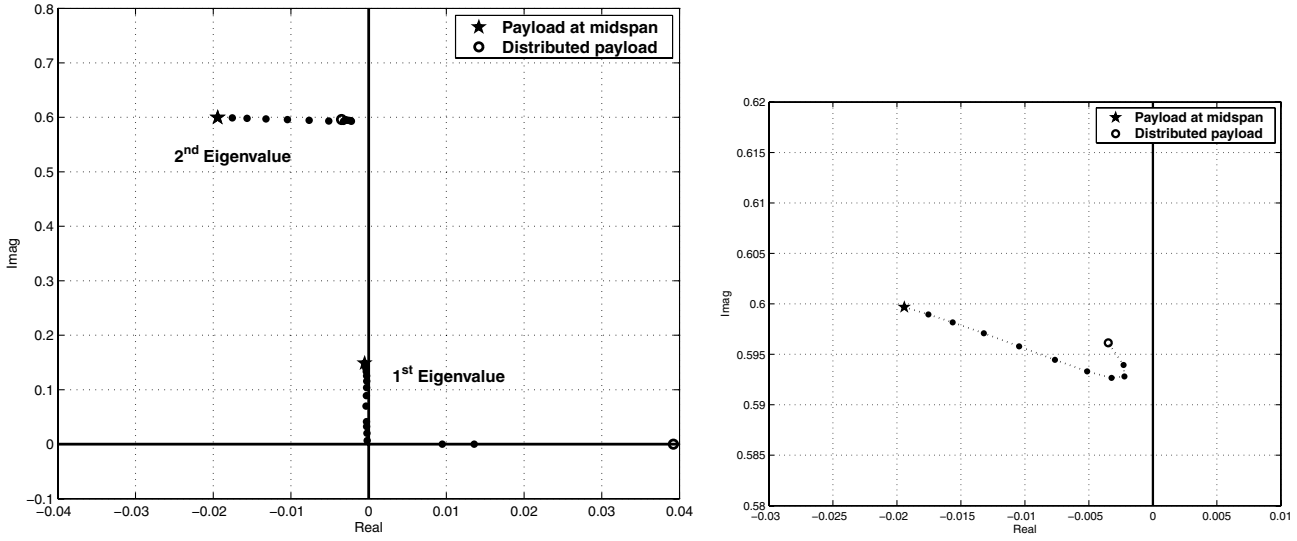

Fig. 3 Root locus of the two lowest eigenvalues (the right figure is zoomed in for the second eigenvalues).

payload is evenly distributed along the whole span of the wing, the wing deflection will be small. However, if it is concentrated at midspan, the wing deforms to a U shape with a much larger tip deflection. Indeed, as the wing deforms to a high U shape, the center of gravity moves up from the beam reference line and the pitch inertia increases. Therefore, a highly flexible flying-wing aircraft is expected to have much more complicated flight dynamic and aeroelastic characteristics because all those aspects are highly coupled to each other due to the high wing flexibility.

The base configuration is given in Tables 1 and 2, and the total payload is arranged along the whole wing span. The wing is divided into 22 finite elements (with 23 nodes). Two cases are compared with each other with same total payload: case 1 with distributed payloads ($m_{\text{dist}} = 17.75/23 = 0.75$ kg) at all the nodes from 1 to 23 and case 2 with a concentrated payload (17.75 kg) at the midspan. (The node at midspan is the 13th node.) Fig. 2 shows the deformed shape of cases 1 and 2 in trim condition. (To be trimmed with a positive static margin, the airfoil for flying-wing aircraft has a negative camber that makes C_{m_0} positive.) The large wingtip deflection is seen in the right part of Fig. 2 due to the concentrated payload at midspan. Case 1 shows an approximately flat (and slightly inverted U) shape with relatively small wing deflection because the payloads are evenly distributed from nodes 1 to 23. Intermediate cases are generated to observe how the eigenvalues change from case 1 to case 2 as the total payload mass is allocated in a symmetric manner at nodes from n_{left} to n_{right}, such that

$$m_{\text{dist}} = \frac{17.75}{n_{\text{right}} - n_{\text{left}} + 1} \tag{29}$$

Figure 3 shows the root locus of the two lowest eigenvalues, and Table 3 shows the eigenvalues for cases 1 and 2. The first eigenvector is related to the yaw and roll attitudes. The second eigenvector is related to the pitch attitude and first symmetric structural bending mode. (The participation of each type of motion in the first and second eigenvectors depends on the payload distribution.)

As the payload gets distributed over a larger portion of the wing span (from $\star$ to $\circ$ in Fig. 3), the first eigenvalue becomes unstable. When the wing deforms to inverted U shapes, the first eigenvalue is real and positive, showing that it loses its dihedral effect. The behavior of the second eigenvalue is more complicated because the payload distribution and the deformed wing shape change the

Table 3 Two lowest eigenvalues of cases 1 and 2 and associated mode descriptions

	Case 1	Case 2	Associated mode
First eigenvalue	0.0392	$-0.0005 \pm 0.1487i$	Yaw and roll attitude modes
Second eigenvalue	$-0.0034 \pm 0.59614i$	$-0.0194 \pm 0.59968i$	Pitch attitude and first symmetric structural bending modes

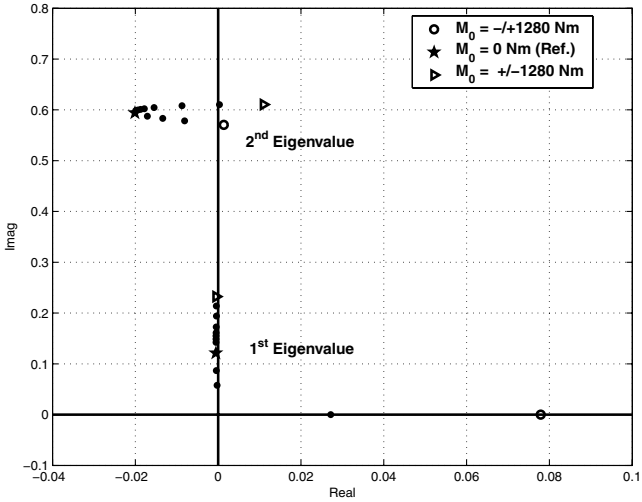

Fig. 4 Root locus of flight dynamic modes depending on the deformed wing shape under applied moments.

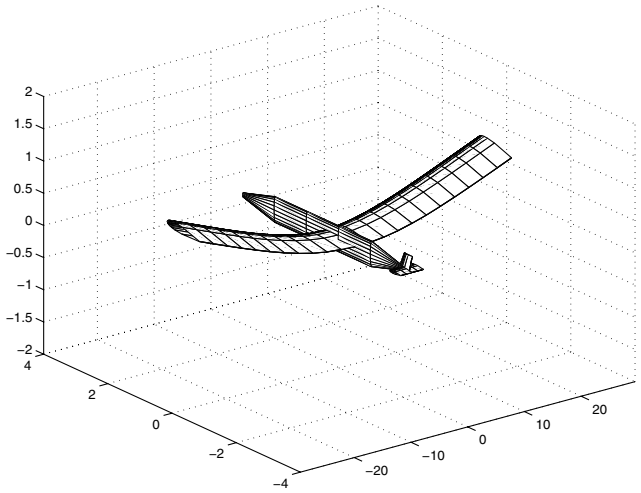

Fig. 5 Trim configurations of conventional aircraft.

location of the center of gravity and the pitch inertia simultaneously. Configurations that are very close to flat are the least stable, but for an inverted U shape, the trend reverses. The deformed U shape due to the concentrated payload at midspan provides more stable flight dynamic modes. But the following study will show that the results are quite sensitive to the change of deformed wing shape that occurs through interaction with the aerodynamic loads.

An additional study is now undertaken to understand the effect of the deformed U shape on each mode for case 2. One way of achieving this shape is applying additional moments at both the 7th and 17th nodes on the right and left wings to adjust the deformed U shape. This is similar to what an active structure might do. To deform the wing to the high U ($\triangleright$) and inverted U ($\circ$) shapes, moments ($M_0 = \pm 1280$ and ∓ 1280 Nm, respectively) are applied. (Intermediate cases are obtained by applying moments between ± 1280 and ∓ 1280 Nm.)

Like the previous result, in Fig. 4, the first eigenvalue becomes unstable for inverted U shapes. However, the second mode behaves highly nonlinearly around the reference configuration ($\star$). Here, both the highly deformed U shape and the less deformed U shape become less stable. This result indicates that the stability of the reference configuration, which is loaded by the concentrated payload at midspan, might be quite sensitive to deformation of the vehicle due to external forces.

A similar result was reported in the Helios mishap report [18]. The phugoid mode of Helios, which can be characterized as a dynamically unstable pendulum mode, is closely related to pitch inertia changes caused by the deformed U shape. It is obvious that the highly deformed U shape has a larger pitch inertia. To maintain the same level of stability, it was noted that the restoring aerodynamic forces and moments should increase with respect to the increased pitch inertia. Otherwise, the phugoid mode becomes less stable.

One difficulty arises in predicting the behavior of the second mode only based on one's insight. The numerical study showed that it is quite complicated and can be highly nonlinear, because the high wing flexibility couples to various aspects: the pitch inertia due to the payload distribution and the deformed wing shape, the location of center of gravity and aerodynamic center of the vehicle, and the aerodynamic force and moment evaluation. This suggests additional numerical studies (described later) to investigate hybrid configurations for a given reference configuration.

B. Flight Dynamic Characteristics of Various Hybrid Configurations

This example might be regarded as somewhat abstract. However, when analyzing a prototype configuration, one can investigate the influence of individual components on the flight dynamic characteristics by introducing numerical variations on the configuration (i.e. a hybrid configuration). As a result, the designer/analyst can understand the effects of individual structural and aerodynamic components on the flight dynamic characteristics, assessing those aspects that agree to the designer/analyst's insight.

Figure 5 shows a trim configuration for the reference configuration given in Tables 4 and 5. The wing, fuselage, and horizontal tail are modeled as beams, and the vertical tail is modeled as a rigid-body component. The wing is located at $3/5$ position of the total fuselage length from the fuselage nose, and the horizontal tail is located at the tip end of the fuselage.

Three hybrid configurations are studied through varying the properties of the fuselage and the horizontal tail:

1) Hybrid configuration 1 is studied for the effect of fuselage mass distribution. The reference configuration has the same value of $[4\ \ 4\ \ 4\ \ 4\ \ 4] = [\mathrm{m}^{(1)}\ \ \mathrm{m}^{(2)}\ \ \mathrm{m}^{(3)}\ \ \mathrm{m}^{(4)}\ \ \mathrm{m}^{(5)}]$, where $\mathrm{m}^{(n)}$ is the mass of nth element in fuselage, and is varied by shifting more weight to the center element [1 1 16 1 1] and more weight in the tips of fuselage [8.5 1 1 1 8.5]. Fig. 6a shows the result. This variation is associated with the change of fuselage inertia and it thus rarely affects wing deformation. As pointed out in the previous study, the second mode is related to pitch inertia and the aerodynamic evaluation. Because

Table 4 Reference-configuration parameters

Parameters	Values	Units
Magnitude of aircraft forward velocity	20	m/s
Flight path angle	0	rad

Table 5 Reference-configuration properties

Properties		Wing	Fuselage	Horizontal tail	Units
m	Mass per unit length	0.75	4.00	0.10	kg/m
ℓ	Total length	55	5	4	m
$d\ell$	Element length	2.5	1	1	m
r/c	Radius/chord length	1	0.5	0.5	m
GJ	Torsional stiffness	1.0×10^4	1.0×10^6	1.0×10^4	Nm^2
EI_2	Vertical bending stiffness	5.0×10^5	2.0×10^6	2.0×10^5	Nm^2
EI_3	Chordwise bending stiffness	4.0×10^6	4.0×10^8	4.0×10^6	Nm^2

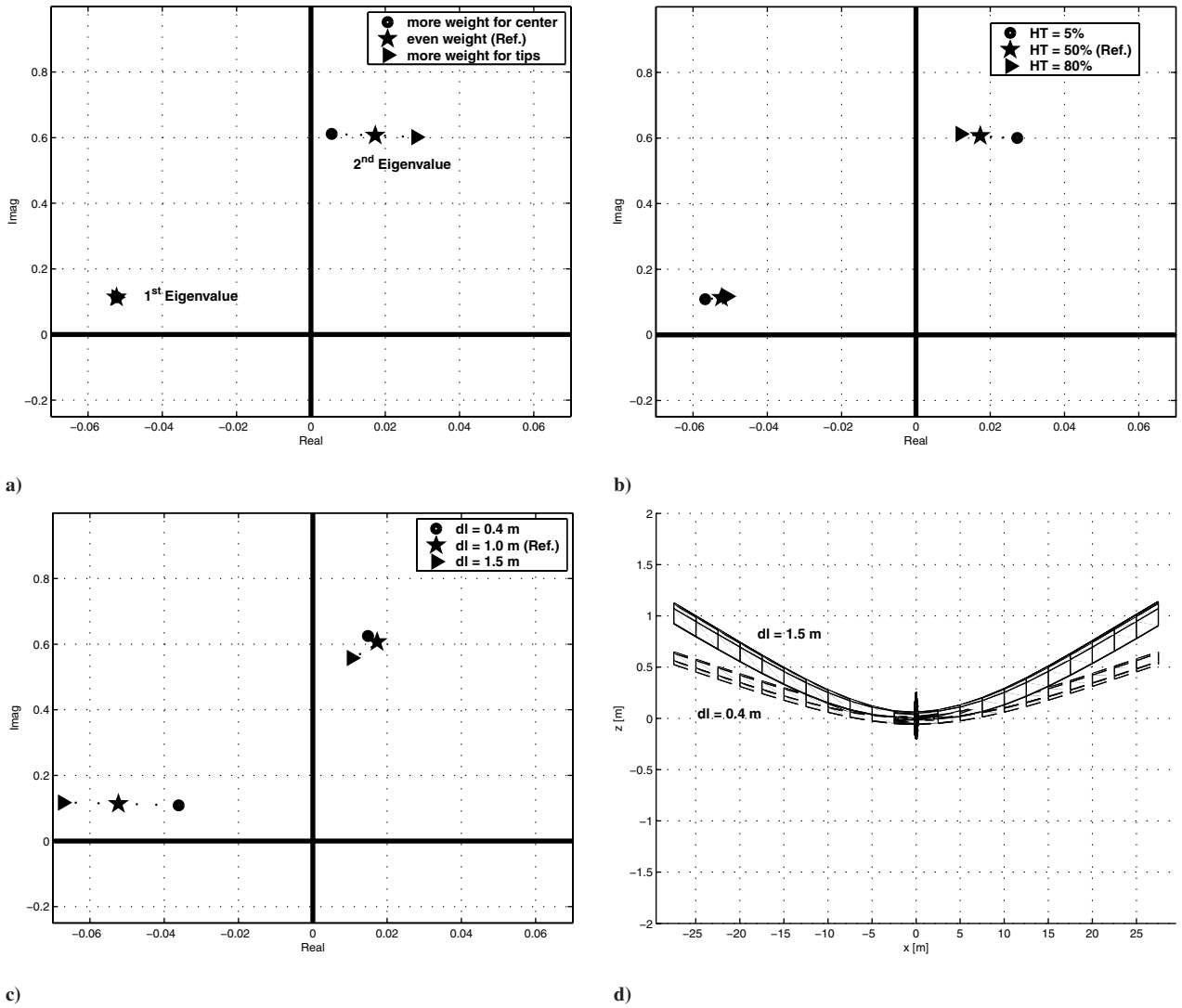

Fig. 6 Root locus for the first and second eigenvalues of the hybrid configurations 1–3 and additional figure for the deformed wing shape of the hybrid configuration 3.

the aerodynamic evaluation rarely changes compared with the increased pitch inertia, the second eigenvalue becomes more unstable when the weight is more toward the tips.

2) Hybrid configuration 2 is studied for the effect of the horizontal tail area (with the same span). Fig. 6b shows the result. (The percentage value is compared with the horizontal tail area with a 1-m chord and a constant 4-m span.) This will estimate the horizontal tail's aerodynamic contribution. As expected, the horizontal tail mainly stabilizes the second mode by providing more aerodynamic damping to the system.

3) Hybrid configuration 3 is studied for the effect of fuselage length (with the total fuselage mass fixed). Fig. 6c shows the result. This variation is associated with direct changes in fuselage inertia and the location of the horizontal tail, and these will modify the fuselage aerodynamic force and moments and horizontal tail's aerodynamic contribution. As the fuselage length increases, the increased pitch inertia will play a negative effect on the second mode, whereas the horizontal tail contributes a positive effect. This leads to nonlinear behavior of the second mode. For the first mode, the longer fuselage leads to a deeper U shape in the trim condition, which ensures more lateral stability. The deformed wing shape for $\mathrm{d}\ell = 0.4$ and 1.5 m are plotted in Fig. 6d.

V. Conclusions

This work presented an analysis methodology for highly flexible aircraft. The structural model was extended to model trim, flight dynamics, and aeroelastic stability of aircraft with structural configurations that can be represented as a collection of beams. This enables one to analyze various possible prototype candidates in the preliminary design process by assessing the effect of individual structural/aerodynamic components and parameters on the flight dynamic characteristics of such aircraft. In this study, for example, two main contributors were taken into consideration in terms of their effect on the flight dynamic characteristics of certain highly flexible aircraft: the effects of the deformed U shape determined by the payload distribution and the effects of fuselage and horizontal tail parameters. The results illustrate the relationship among various design parameters and the flight dynamics. It can thus suggest possible design improvements in terms of certain parameters or configurations to achieve better flight dynamic characteristics.

In addition, because the wing is highly flexible, the aerodynamic formulation directly interacts with the structural wing deflection. Small changes in the parameters and configuration affect the trim condition and yield a distinctive trim condition for such highly flexible aircraft because those effects are so strongly coupled to each other.

Acknowledgments

This work was supported in part by the NASA Dryden Flight Research Center, with Kevin Walsh as the technical monitor. Technical discussions with Dana Taylor of Aerovironment, Inc., are gratefully acknowledged.

References

[1] Zerweckh, S. H., von Flotow, A. H., and Murray, J. E., "Flight testing a highly flexible aircraft—Case study on the MIT Light Eagle," *Journal of Aircraft*, Vol. 27, No. 4, 1990, pp. 342–349.

[2] van Schoor, M. C., and von Flotow, A. H., "Aeroelastic Characteristics of a Highly Flexible Aircraft," *Journal of Aircraft*, Vol. 27, No. 10, Oct. 1990, pp. 901–908.

[3] Waszak, M. R., and Schmidt, D. K., "Flight Dynamics of Aeroelastic Vehicles," *Journal of Aircraft*, Vol. 25, No. 6, June 1988, pp. 563–571.

[4] Schmidt, D. K., and Raney, D. L., "Modeling and Simulation of Flexible Flight Vehicles," *Journal of Guidance, Control, and Dynamics*, Vol. 24, No. 3, 2001, pp. 539–546.

[5] Patil, M. J., Hodges, D. H., and Cesnik, C. E. S., "Nonlinear Aeroelasticity and Flight Dynamics of High-Altitude Long-Endurance Aircraft," Proceedings of the 40th Structures, Structural Dynamics and Materials Conference, Saint Louis, MO, AIAA Paper 99-1470, Apr. 1999, pp. 2224–2232.

[6] Patil, M. J., Hodges, D. H., and Cesnik, C. E. S., "Nonlinear Aeroelastic Analysis of Complete Aircraft in Subsonic Flow," *Journal of Aircraft*, Vol. 37, No. 5, Sept.–Oct. 2000, pp. 753–760.

[7] Patil, M. J., and Hodges, D. H., "Static Output Feedback Control of Nonlinear Aeroelastic Response of a SlenderWing," *Journal of Guidance, Control, and Dynamics*, Vol. 25, No. 2, Mar.–Apr. 2002, pp. 302–308.

[8] Patil, M. J., and Hodges, D. H., "Flight Dynamics of Highly Flexible Flying Wings," *Journal of Aircraft*, Vol. 43, No. 6, 2006, pp. 1790–1799. doi:10.2514/1.17640

[9] Hodges, D. H., "A Mixed Variational Formulation Based on Exact Intrinsic Equations for Dynamics of Moving Beams," *International Journal of Solids and Structures*, Vol. 26, No. 11, 1990, pp. 1253–1273. doi:10.1016/0020-7683(90)90060-9

[10] Hodges, D. H., "Geometrically Exact, Intrinsic Theory for Dynamics of Curved and Twisted Anisotropic Beams," *AIAA Journal*, Vol. 41, No. 6, June 2003, pp. 1131–1137.

[11] Drela, M., "Integrated Simulation Model for Preliminary Aerodynamic, Structural, and Control-Law Design of Aircraft," *40th Structures, Structural Dynamics and Materials Conference*, AIAA, Reston, VA, Apr. 1999, pp. 1644–1656.

[12] Meirovitch, L., and Tuzcu, I., "Unified Theory for the Dynamics and Control of Maneuvering Flexible Aircraft," *AIAA Journal*, Vol. 42, No. 4, 2004, pp. 714–727.

[13] Meirovitch, L., and Tuzcu, I., "Time Simulations of the Response of Maneuvering Flexible Aircraft," *Journal of Guidance, Control, and Dynamics*, Vol. 27, No. 5, 2004, pp. 814–828.

[14] Meirovitch, L., "Hybrid State Equations of Motion for Flexible Bodies in Terms of Quasi-Coordinates," *Journal of Guidance, Control, and Dynamics*, Vol. 14, No. 5, 1991, pp. 1008–1013.

[15] Garcia, J. A., "Numerical Investigation of Nonlinear Aeroelastic Effects on Flexible High-Aspect-Ratio Wings," *Journal of Aircraft*, Vol. 42, No. 4, 2005, pp. 1025–1036.

[16] Snyder, R. D., Hur, J. Y., Strong, D. D., and Beran, P. S., "Aeroelastic Analysis of a High-Altitude Long-Endurance Joined-Wing Aircraft," 46th AIAA/ASME/ASCE/AHS/ASC Structures, Structural Dynamics, and Materials Conference, Austin, TX, AIAA Paper 2005-1948, Apr. 2005.

[17] Peters, D. A., Karunamoorthy, S., and Cao, W.-M., "Finite State Induced Flow Models, Part 1: Two-Dimensional Thin Airfoil," *Journal of Aircraft*, Vol. 32, No. 2, Mar.–Apr. 1995, pp. 313–322.

[18] Noll, T. E., Brown, J. M., Perez-Davis, M. E., Ishmael, S. D., Tiffany, G. C., and Gaier, M., "Investigation of the Helios Prototype Aircraft Mishap," Vol. 1, NASA, Jan. 2004,